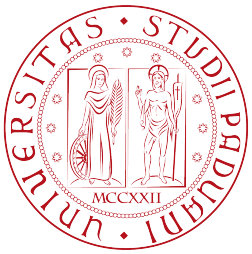

Università degli Studi di Padova

Dipartimento di Fisica e Astronomia
"Galileo Galilei"
Corso di Laurea in Fisica

Tesi di Laurea

Finding the gamma-ray counterparts of gravitational wave events with Fermi LAT

Laureanda:
Arianna Coppola

Relatore:
Prof. Denis Bastieri

Anno Accademico 2015-2016

Contents

Introduction

Gravitational waves were directly detected for the first time on September 14, 2015 by both the twin Laser Interferometer Gravitational-Wave Observatory (LIGO) detectors, the largest and the most sensitive interferometers ever built. A second gravitational wave transient was observed on December 26, 2015. This discovery, as well as confirming the predictions made by Albert Einstein in 1916, has opened a new window onto the Universe.

Several black hole candidates had been previously identified through electromagnetic observations, but these signals from gravitational waves have demonstrated the existence of binary stellar-mass black hole systems and have also represented the first detection of two black holes colliding and merging into one.

Moreover, some of the most promising astrophysical sources of gravitational waves are also expected to produce broadband electromagnetic emission and neutrinos. This has led to exciting new follow-up programs that connect gravitational and electromagnetic observations.

The purpose of this thesis is therefore to focus on the collaboration between LIGO and the *Fermi* Gamma-ray Space Telescope. *Fermi*'s main instrument, the Large Area Telescope (LAT), provides a continuous and uniform monitoring of the Universe in the gamma-ray band, from 30 MeV to more than 300 GeV. Furthermore, thanks to its observation "scanning" mode, any potential source of gravitational waves will enter the LAT's Field of View within three hours.

Our aim is then to develop a tool able to identify, among all the gamma-ray LAT sources, those that may represent counterparts of gravitational wave events, starting from the so-called "banana plots", which are provided after the gravitational wave detection and contain the probability that the signal has come from any direction in the sky.

The first chapter presents an overview of the *Fermi* LAT and LIGO missions, along with a description of the respective detectors, as well as, on the one hand, a summary of gamma-ray sources and, on the other hand, the major features of the two gravitational wave events.

The second chapter introduces *Fermi* data analyses. In the first section, the activity of Flare Advocates, who are in charge of prompt daily reports of gamma-ray sources observed by the LAT, is discussed; the second section contains a detailed description of HEALPix, the method of sphere pixelation useful to deal with the large amount of data of the LAT and LIGO and consequently with our tool.

Finally, the third chapter presents the banana plots and the basic Python code of the tool through some helpful functions included in the HEALPix software package.

Chapter 1

LAT and LIGO

1.1 *Fermi* LAT mission

Fermi Gamma-ray Space Telescope (FGST), formerly called GLAST (Gamma-ray Large Area Space Telescope), is a satellite belonging to the National Aeronautics and Space Administration (NASA), whose main purpose is to detect gamma rays from the whole sky. It was launched into a near-earth orbit (at an altitude of $\sim 550\,\mathrm{km}$ and a revolution period of $\sim 90\,\mathrm{min}$) on June 11, 2008 and began its sky survey on August 11, 2008 — most of the information about the *Fermi* LAT included in this section is available in Michelson et al. (2010 [16]).

Fermi is a mission supported by NASA and the U.S. Department of Energy (DOE), along with important contributions from more than 400 academic institutions and partners in France, Italy, Japan, Sweden, Germany and from observatories in Great Britain and Australia.

Fermi's primary instrument is the Large Area Telescope (LAT), sensitive to gamma rays in the energy range from $\sim 30\,\mathrm{MeV}$ to more than $300\,\mathrm{GeV}$, while X-rays and gamma rays with energies between $8\,\mathrm{keV}$ and $40\,\mathrm{MeV}$ are detectable by the Gamma-ray Burst Monitor (GBM), that complements the LAT for observations of high-energy transients.

Previous high-energy gamma-ray observations were made by the ESA's satellite COS-B and by NASA's EGRET - on the Compton Gamma-Ray Observatory - and SAS-2.

Moreover, gamma-ray research is completed by ground-based telescopes — sensitive to energies above $\sim 100\,\mathrm{GeV}$ — such as H.E.S.S. in Namibia, VERITAS in Arizona, Magic in La Palma (Canary Islands), Cangaroo in Australia, Milagro in New Mexico.

The central aim of *Fermi* mission is to find out the origin of gamma rays, studying already detected sources and looking for new ones, located both in the Milky way and in other galaxies, and identifying sources of unknown nature, in particular those seen by EGRET. *Fermi* is also trying to explain the processes that could be related to high-energy gamma-ray emission, including the origin of cosmic rays. Furthermore, the *Fermi* LAT represents a unique instrument for dark matter indirect searches, since its annihilation or decay would produce detectable particles, including gamma rays in the sensitivity range of the LAT.

1.1.1 The LAT detector

The LAT is a wide field-of-view pair-conversion telescope. In fact, pair conversion is the main process by which gamma rays with energies greater than $\sim 10\,\mathrm{MeV}$ interact with matter: after the photon is absorbed because of its interaction with the electromagnetic field of a nucleus, an electron-positron pair is created.

The instrument, as shown in Fig. 1.1, consists of a 4×4 of 16 modules; each of them contains a Tracker module (1) and a Calorimeter module (2). An Anticoincidence Detector

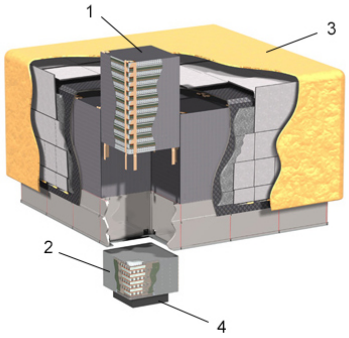

Fig. 1.1: A cut-away of the *Fermi* LAT instrument.
Credits: NASA.

(ACD) (3) covers the Tracker modules and a Data Acquisition System (DAQ) (4) is located underneath the array. These four subsystems are designed to work together in order to detect gamma rays and to reject intense background signals from cosmic rays (the ratio of cosmic rays to gamma rays entering the LAT varies from 10^5:1 to 10^6:1).

According to the full explanation available at NASA — Fermi Spacecraft and Instruments (2008 [17]), an incoming gamma ray entering the LAT passes through the ACD and will not produce signals, as the ACD is sensitive only to cosmic rays. The Tracker is made up by alternating layers of tungsten foils and trays of Silicon strip detectors (SSD). Due to the interaction between the gamma ray and tungsten, an electron-positron pair is produced; the SSDs measure then the trajectories of electrons and positrons allowing the LAT to determine the arrival direction of the gamma ray.

The energy of the gamma ray is instead estimated in the Calorimeter, made of CsI crystals, that provides measures of the pairs energy: the intensity of light emitted from its crystals is proportional to the energy of the incoming particles. The Tracker and the Calorimeter present a total thickness of about 10 radiation lengths[1] at normal incidence, divided into $\sim$ 8.5 and $\sim$ 1.5 radiation lengths in the Calorimeter and in the Tracker respectively.

The ACD contains specific plastic tiles that produce flashes of light when hit by charged particles such as cosmic rays (differently from gamma rays, which are electronically neutral); the information of an incoming cosmic ray is therefore transmitted to the DAQ in order to reject the related signal. 99.97 % of unwanted signals are discarded.

The DAQ, consisting of specialized electronics and microprocessors, finally relays data to the ground for further processing. It is able, in addition, to do on-board searches for Gamma-Ray Bursts (GRBs), even though the main instrument on *Fermi* detecting GRBs is the GBM.

LAT's Field of View (FoV)[2], equal to 2.4 sr, covers approximately 20 % of the sky at any time; moreover, *Fermi* is able to uniformly monitor the whole celestial sphere every two orbits around Earth (every about three hours) through LAT's primary sky survey mode, the "scanning" (or "rocking") mode: the normal to the front of the instrument rocks first from zenith to the north pole of the orbit and, on the following orbit, from zenith to the south pole; in this way, the satellite alternates the scanned emisphere after every orbit.

[1] The distance covered by electrons and positrons at which their energy is reduced to $\frac{1}{e}$ of the original energy.

[2] Size of the sky region from which the detector collects data.

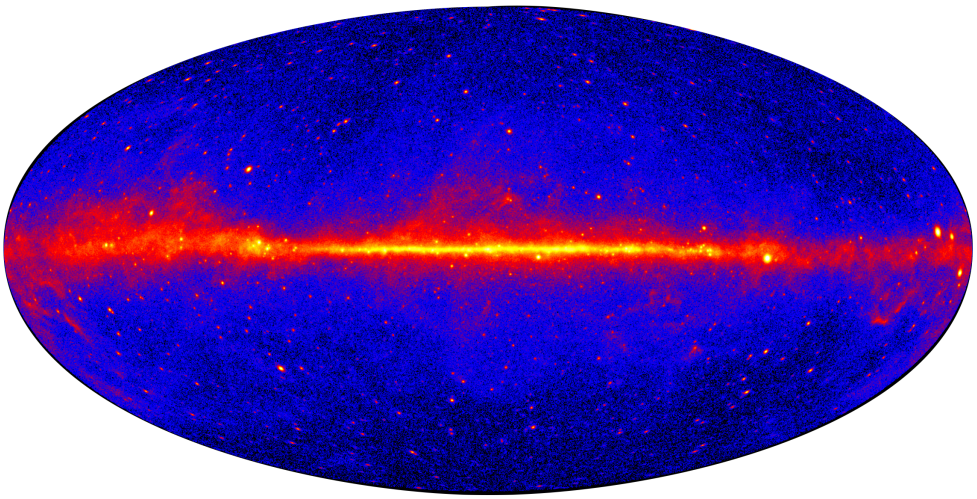

Fig. 1.2: Gamma-ray sky as seen by the LAT according to the data collected over five years (2008-2013) and related only to photons with energies greater than 1 GeV and converted at the front of the Tracker.
Credits: NASA/DOE/Fermi LAT Collaboration.

Pointed observations are also possible: for example, if the GBM detects a gamma-ray burst above a given threshold, since it is able to inform the LAT of the burst position, the LAT is autonomously re-pointed in order to keep the burst inside the FoV for the following five hours.

The *Fermi* LAT has introduced some key improvements in performance, mainly due to newer technologies, if compared with the previous telescopes COS-B, SAS-2 and EGRET; they include a larger effective area[3] thanks to the great FoV, a better angular resolution[4] and background rejection and the improved DAQ.

1.1.2 LAT results

Fig. 1.2 is the result of the first five years of data collected by the *Fermi* LAT. It is a false color counts map, showing for each point in the sky the number of photons that reached the instrument from that direction. The number of photons increases from blue (few photons) to yellow (many photons), passing through red. The plot is in galactic coordinates, with the center of the Galaxy at the center of the map and longitude increasing to the left (eastward).

The image clearly presents two types of gamma-ray sources: diffuse emission, mostly coming from the central plane of the Milky Way, and point sources, that appear as bright spots here and there on the blue background. Analyses of LAT data have shown that gamma rays are produced by a lot of different sources, both in our Galaxy and in the Universe, mainly including[5] (Michelson et al. 2010 [16]):

[3]The number of photons detected divided by the source flux. LAT effective area is a function of photon energy and inclination angle; its highest value for normal incidence photons is $\sim 9200\,\mathrm{cm}^2$, while EGRET's one is $\sim 1500\,\mathrm{cm}^2$.

[4]LAT angular resolution is $< 3.5°$ (for a single photon with energy of $\sim 100\,\mathrm{MeV}$) and $< 0.15°$ (for a single photon with energy $> 10\,\mathrm{MeV}$), while EGRET's one is 5.8° (for a single photon with energy of $\sim 100\,\mathrm{MeV}$).

[5]The number of detected sources refers to 3FGL, that is the third LAT catalog, containing 3033 sources

Galactic Diffuse Emission This corresponds to the bright central band of Fig. 1.2. Here gamma rays are generated mostly by the interactions of cosmic rays with interstellar gas and the interstellar radiation field; in the former case, a cosmic-ray proton interacts with an interstellar proton producing π^0 that decays in photons[6], or the deceleration of a cosmic-ray electron in the proximity of a gas atom causes photons emission via bremsstrahlung. In the latter case, through inverse Compton scattering, a cosmic-ray high-energy electron gives energy to an interstellar low-energy photon (for example, a Cosmic Microwave Background photon), with the outcome of a high-energy photon.

Pulsars (PSRs) Particles accelerated to high energies in the pulsar magnetosphere lead to photons production by means of a combination of curvature radiation, synchrotron radiation and inverse Compton scattering. 167 detected, included binary pulsars.

Globular Clusters Along with several binary systems, these old stars clusters of our Galaxy contain many millisecond pulsars (MSPs), that are believed to be their primary gamma-ray sources. The first to be detected was 47 Tucanae (NGC 104), 4 kpc away[7]. 15 detected.

Supernova Remnants (SNRs) *Fermi* observations seem to confirm the hypothesis that supernovae not only produce cosmic rays, but that they are the primary sources of cosmic rays in normal galaxies; in order to test this hypothesis, searches for gamma-ray emission from star-forming galaxies are carried out, as the birth of stars is facilitated by supernovae. Gamma rays are therefore produced as explained above if the remnant is placed nearby a molecular cloud. 23 detected, including middle-aged $\sim 10^4$ yr and young $< 10^3$ yr remnants.

Binary Sources Four of those detected by the LAT consist of a massive star and a compact object, which could be a neutron star or a black hole; the probable process causing gamma rays production is again the inverse Compton scattering, involving stellar photons and electrons accelerated in the proximity of the compact object or maybe particles accelerated in a relativistic jet, as in the case of the microquasar Cygnus X-3. 4 sources plus the binary Eta Carinae (consisting of two massive stars) detected.

Blazars, Quasars and Radio Galaxies These type of active galaxies[8] present a relativistic jet flowing out from the central core, representing the gamma-ray emission source, even though they mostly emit in the radio band. The angle between the line-of-sight and the jet axis increases from blazars to radio galaxies. The extra-galactic high-energy gamma-ray sky is anyway dominated by blazars; a possible process for the gamma rays production involves high-energy electrons in the jet interacting with low-energy photons from the synchrotron radiation produced by electrons (this case is referred to as synchrotron self-Compton) or from an external source (external Compton). Blazars are divided into two spectrally distinct populations: Flat Spectrum Radio Quasars (FSRQs), characterized by higher photon index[9], and BL Lacertae (BL Lac) objects, with a lower photon index. 660 BL Lac, 484 FSRQs, 16 Radio Galaxies, 573 blazar candidates detected.

---

above 4σ significance, detected in the first four years in the 100 MeV-300 GeV range. It is also called 4-year Point Source Catalog (Fermi Science Support Center 2016 [9]).

[6] π^0 production: $p + p \to p + p + \pi^0$, π^0 primary decay: $\pi^0 \to 2\gamma$.

[7] 1 pc $\cong$ 3.26 ly.

[8] Typically elliptical galaxies presenting a small central region, probably a black hole, of very bright emission compared to the rest of the galaxy.

[9] See Section 2.1.

Normal Galaxies Large Magellanic Cloud (LMC), Small Magellanic Cloud (SMC) and Andromeda (M31), among the nearest galaxies to the Milky Way, have been detected. Most of the other galaxies of the Universe are too far to be detectable, but the same gamma-ray processes present in the Milky Way are expected to take place. In the LMC, for example, gamma rays seem to be probably produced by cosmic rays accelerated in the 30 Doradus star forming region.

Gamma-Ray Bursts (GRBs) They basically consist in collimated, super-relativistic (with initial Lotentz factor $\gamma \cong 10^2$-10^3, which means $\beta \cong 0.99995$-0.9999995) blast waves emitting in the gamma-ray band and also in the X-ray and in lower-energy bands. They are generally divided into two categories (Berger 2014 [6]): long-duration GRBs (the emission lasts more than 2 s and usually less than 100 s-500 s), probably originated in star-forming regions from a massive star collapse with the consequent formation of a black hole; and short-duration GRBs (lasting less than 2 s), thought to be maybe produced during compact object binary mergers (two supernovae or a black hole and a supernova), even though many more efforts are needed in order to understand GRBs mechanisms. Actually, a third type of bursts exists: ultra-long duration GRBs, lasting several thousands of seconds. GRBs are mainly studied by the *Fermi* GBM.

According to Michelson et al. (2010 [16]), other gamma-ray sources are the Sun, due to the interaction of cosmic-ray protons with the solar atmosphere or inverse Compton scattering between cosmic-ray electrons and positrons and the solar radiation field, and the Moon, where cosmic rays interact with the regolith surface. Another source is the extragalactic background (EGB), a diffuse gamma-ray emission mainly due to unresolved extragalactic sources either because too far or too faint to be detected as pointlike sources. Moreover, the LAT detected for the first time gamma-ray emission from Seyfert galaxies, that are typically spiral galaxies with jets whose power seems to be comparable to that of blazars, contrary to what it was believed before *Fermi* observations.

3FGL contains also 12 Pulsar Wind Nebulae (PWNe)[10], including for example the Crab Nebula and Vela-X.

Sources for dark matter (DM) could lie in the Galaxy halo[11] objects, in particular DM clumps as predicted by N-body simulations and Dwarf Spheriodal Galaxies (DSphs), that self gravitate and orbit about the Milky Way and probably do not contain many gamma-ray known sources; moreover, other candidate sources are galaxy clusters. Data have been collected as well from an all-sky region with the Galactic plane removed, in order to reduce the Galactic Diffuse Emission background, and from the Galactic Center, that is believed to host a great concentration of dark matter (Michelson et al. 2010 [16]).

DSphs are currently the most promising sources for DM. Moreover, DM annihilation may occurr in galaxy clusters (Charles et al. 2016 [7]). Anyway, searches are still in progress and advances and cross checks are expected thanks to more and more LAT data.

1009 unassociated sources are still present in the 3FGL catalog. On the other hand, the *Fermi* LAT have found out sources that were not present in the EGRET catalogs; the third EGRET catalog, for example, contains only 271 sources, plus 27 candidate blazars and 170 unidentified sources (Michelson et al. 2010 [16]). *Fermi* successful results are possible thanks to its strong performance improvements; FA activity[12] is of great importance as well. Examples of relevant detected sources are the extraordinary outburst from blazar 3C 454.3,

[10] Nebulae composed of a wind of charged particle sorrounding some young pulsars; they are the remnants of the supernova from which the pulsar originates.

[11] The halo of the Galaxy is a spherical region around the Milky Way cointaing both single stars and globular clusters, gas and probably dark matter.

[12] See Section 2.1.

the detection of a nova in V407 Cygni, the binary star system 1FGL J1018.6-5856, the above-mentioned microquasar Cygnus X-3 (Bastieri et al. 2011 [5]; Ciprini et al. 2012 [8]).

1.2 LIGO mission

The Laser Interferometer Gravitational-Wave Observatory (LIGO) is the largest gravitational wave observatory in the world whose aim is the direct detection of gravitational waves (GW) that reach Earth from the Universe.

Most of the information included here and in Section 1.2.1 about LIGO is available at LIGO Lab website ([13]).

Currently LIGO is composed of two identical interferometers working in unison, located respectively in Livingston (Louisiana) and in Hanford (Washington) — with $\sim 3000\,\mathrm{km}$ separating the two detectors. It is operated by the California Institute of Technology (Caltech) and the Massachusetts Institute of Technology (MIT) and funded by the U.S. National Science Foundation. Australia, Germany and the United Kingdom contributed financially to the construction of LIGO's detectors.

In addition, Virgo, a 3 km interferometer placed near Pisa (Italy), will soon provide LIGO's partners with information about candidate gravitational wave signals. Furthermore, the GEO600 detector in Hannover (Germany) cooperates in the LIGO Scientific Collaboration (LSC), in which dozens of scientific institutions around the world take part. A recent Memorandum of Understanding has been signed between LIGO and *Fermi*, in order to hopefully observe sources of gravitational waves in gamma rays.

Many key questions concerning GW and Einstein's General Relativity theory may find the answer in LIGO's outcomes; measures could probably give us more details not only about GW and black holes properties, but also about the formation, evolution and collapse of stars. Moreover, it is hoped to understand whether General Relativity is actually the correct theory for gravity and to identify its validity limits, especially those about strong-gravity conditions — conditions which are typically found, for example, in black holes systems.

1.2.1 LIGO's interferometers

Gravitational waves, according to Einstein's prediction in 1916, consist in distortions in space-time caused by accelerating masses; once generated, these waves propagate from the source at the speed of light. The strongest gravitational waves are produced by catastrophic, greatly energetic processes such as colliding black holes, neutron stars orbiting each other, white dwarfs or neutron stars coalescence, supernovae and the birth of the Universe itself, whose GW remnants still fill it.

The first indirect proof of the existence of GW was given by Joseph Taylor and Russel Hulse, who in 1974 discovered 40 new pulsars by the Arecibo telescope in Puerto Rico. One of them, PSR1913+16, was found out to be a binary pulsar, that is two neutron stars orbiting each other, so a typical GW source; Taylor and Hulse measured the variation in the orbital period of the system over eight years, since, as it was predicted by General Relativity, the emission of gravitational radiation would decrease the energy of the stars with a consequent orbit shrinkage and a period reduction. The emerging results were in agreement with Einstein's prediction. Data have been showing this agreement for 40-years monitoring the pulsar until today.

In order to directly detect them, istruments have to be sensitive to minimal fluctuations in space-time, which can be as small as $10^{-19}\,\mathrm{m}$; LIGO's detectors have the necessary resolution needed for this purpose.

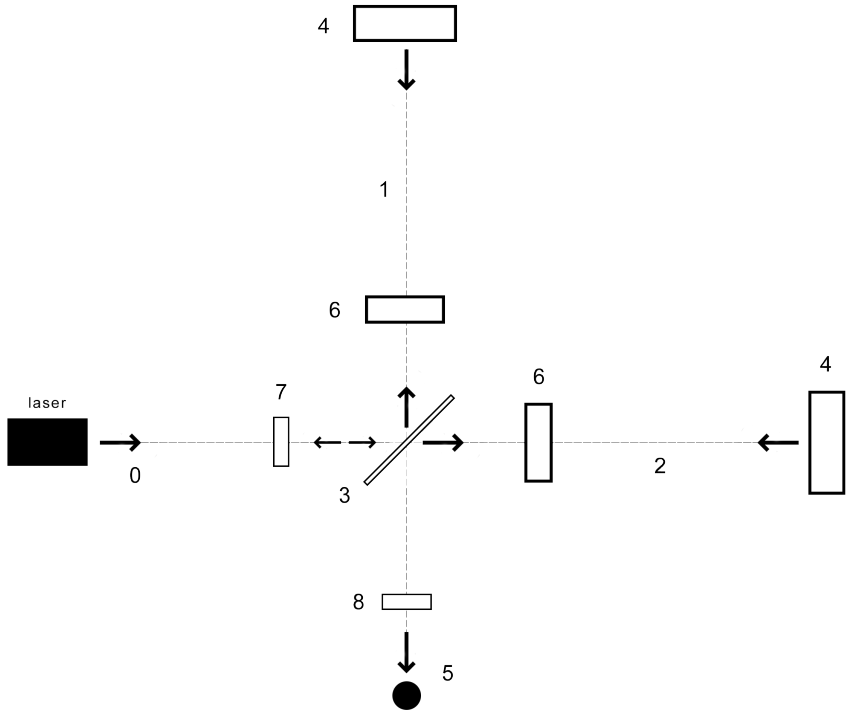

Fig. 1.3: Top view of the basic scheme of LIGO's interferometer. Not to scale.

Actually, only recently LIGO has reached such precision levels: while the original interferometers (the so-called Initial LIGO, iLIGO) were completed in 1999, the current improved version (Advanced LIGO, aLIGO) was built between 2010 and 2014. During the first round of data collection, that took place between 2002 and 2010, no gravitational waves were detected; on September 14, 2015, only few days after the very beginning of the search with the new 10 times more sensitive aLIGO, the first direct detection of gravitational waves was made. The improved LIGO is able to record GW 10 times farther away than the first detectors, that is to record gravitational waves coming from a volume around Earth 1000 times bigger, that cointains a lot more potential sources which could be detected by the instruments. This huge improvement really made the difference between iLIGO and aLIGO.

Nevertheless, the renovation process has not stopped: continuous efforts are being made in order to achieve always better performances, until LIGO reaches the "design sensitivity", expected around 2020.

LIGO's interferometers are essentially Michelson interferometers — like the one used in the Michelson-Morley experiment in 1887 — with more sophisticated features and bigger sizes that allow LIGO to reach a high precision in GW detection. Due to these characteristics, LIGO is classified as a Dual Recycled, Febry-Perot Michelson Interferometer.

Each of LIGO's twin interferometers is composed of two straight and level 4 km long steel vacuum arms (1 and 2 in Fig. 1.3), 1.2 m wide in diameter, arranged in the shape of an L.

The operating principle is similar to that of Michelson's instrument. An incoming laser beam (0) is split into the two arms by a beam splitter mirror (3); each beam travels along one of the tubes until it reaches a mirror (called "test mass") (4), where it is reflected. The

two reflected rays meet again and merge back at the beam splitter; the single final ray is then addressed to the photodetector (5).

Gravitational waves produce continuously stretching and squeezing in the size of an object; therefore, the consequence of a GW approaching the interferometer would be respectively a decrease in length of arm 1 (that is, the distance between the splitter and the mirror at the arm's extremity) and an increase in that of arm 2 and vice-versa an istant later. This back-and-forth lengthening and shortening process would last until the wave has passed.

The different path lengths the two split beams have travelled cause a phase difference between the beams themselves when they re-merge at the splitter, producing alternatively constructive and destructive interference. This makes the laser intensity at the photodetector vary with time and this finally appears as a flicker of light in the photodetector.

The sensitivity to changes in length of an interferometer increases with the distance covered by the laser beams and therefore with the length of the arms. However, LIGO's arms — although more extended than those of Michelson's interferometer, which had arms 11 m long — are not sufficient to detect the tiny length fluctuations produced by a GW. LIGO includes indeed a modification called "Fabry-Perot cavities", obtained by adding two more mirrors (6) near the splitter. Each two-mirrors system is made to reflect the laser beam 280 times along the 4 km "cavity" before it finally combines with that of the other arm; as a consequence, LIGO's sensitivity is increased due to the longer time the laser is stored in the tubes and because the rays cover not a 4 km, but a 1120 km distance.

While sensitivity to vibrations increases with increasing lengths, LIGO's resolution is improved by the laser power: a major number of photons entering the detector means a sharper interference pattern and so a better interference valuation. The needed power for LIGO's full sensitivity operation is 750 kW. Since building such powerful lasers represents almost an impossible task, LIGO uses, in addition to a 200 W laser that actually enters the interferometer, other extra mirrors, called "power-recycling" mirrors (7)[13], placed between the laser source and the splitter. Both the recycling mirrors and the splitter are only partly reflective: this allows most of the rays coming from the arms not to be reflected by the splitter and directed to the photodetector, but to pass through the splitter and travel towards the recycling mirror. Here they are reflected again and re-enter the arms, thus adding to previously present photons and therefore resulting in a great power boost.

Finally, "sygnal-recycling" mirrors (8) enhance, with a mechanism similar to that of power-recycling mirrors, the output signal.

The vacuum created inside the interferometer's arms (the pressure is equal to 10^{-12} times the value it has at sea level) is necessary in order to prevent noise in the tiny distance changes that could result from air molecules hitting the mirrors — due to Brownian motion — and making them move. Moreover, the index of refraction of the air could modify the laser path and light could be scattered in random directions.

Lastly, the tubes are covered by a ~ 3 m wide and ~ 3.7 m tall concrete upholstery. This, together with the seismic isolation system, has the purpose of isolating the arms from as many environmental vibrations as possible. Despite the two interferometers are placed in isolated locations (LIGO Livingston in a pine forest and LIGO Hanford in an arid steppe region), many disturbances may reach them. In fact, due to LIGO's high sensitivity, both near (such as acoustic noise caused by trucks passing on nearby roads) and far vibrations (produced for example by earthquakes occurring in any place of the Earth) could move test masses enough to hide a GW signal.

The active isolation system (Internal Seismic Isolation, ISI, not present in iLIGO)

[13] In Fig. 1.3 only one is shown even if multiple mirrors are used.

provides the interferometer with devices that perform counter movements to undesired ground vibrations; additionally, test masses are suspended at a 4-stage pendulum (iLIGO had a single pendulum) that helps to keep the mirror steady.

aLIGO's mirrors have also a very big mass (40 kg), compared with that one (11 kg) of iLIGO's mirrors, in order to reduce noise coming from the laser hitting the mirror itself, which could cause a movement and a change in the shape of the mirror.

The identical and widely separated interferometers system contributes itself to reduce background noise: each of them is able to detect in the same way a GW, differently from disturbance signals. In addition to the isolation system, it is essential that the two instruments work together to confirm each other's detections.

Furthermore, last February the approval for the costruction of a third LIGO interferometer in India was announced.

1.2.2 LIGO results

The first LIGO's observing run, called O1, started on September 12, 2015 and ended on January 19, 2016. The O1 data set analysis was completed in August 2016 and contained two GW detections related to black holes merger: GW150914 (initially called G184098) and GW151226[14]. The significance of the two events resulted to be greater than 5σ, corresponding to a false-alarm probability of less than 1 in 5×10^6 (equivalent to less than 1 event in $\sim 200\,000$ yr). Information included here about GW150914 and GW151226 detections is available in Abbott et al. (2016a [1]) and Abbott et al. (2016b [2]) respectively.

The third most significant binary black hole candidate is GW151012, later called LVT151012 (Abbott et al. 2016b [2]), even though this signal has not been identified as an unambiguous detection due to its lower significance level.

O2 run is going to start in September 2016 and last about six months.

Both GW150914 and GW151226 signals have been identified with gravitational waves generated by two stellar-mass black holes merging to form a single black hole. In order to validate this result, a lot of investigations of instrumental and environmental disturbances were performed, giving no evidence which might suggest that the signals could be an instrumental effect. Moreover, the observations confirm predictions of General Relativity for a binary black hole system. A first consistency check involves the mass and spin of the final black hole, as in General Relativity the end product of a black hole binary coalescence is a Kerr black hole, which is fully described by its mass and spin. All the analyses that have been carried out show no evidence of disagreement from General Relativity.

The measured difference between the arm lengths L_1 and L_2 of the interferometer, produced by a passing gravitational wave, is equal to $\Delta L(t) = \delta L_1 - \delta L_2 = h(t)L$, where h is the gravitational-wave strain amplitude projected onto the detector (shortly, the strain). This differential length variation alters the phase difference between the two light beams in the arms, resulting in an optical signal, proportional to the strain, to the output photodetector.

Fig. 1.4 shows the evolution in time of the strain for GW150914, as detected by the LIGO Hanford (H1, left column panels) and Livingston (L1, right column panels) interferometers.

In the first row the measured signal is visible. The right panel also compares L1 and H1 signals, with the H1 data shifted in time by $6.9^{+0.5}_{-0.4}$ ms (as the signal arrived first at L1 and then, travelling at the speed of light, reached H1 after this time interval) and inverted (to

[14]The name of GW signals is composed of the letters "GW" followed by the discovery date in the yy-mm-dd format.

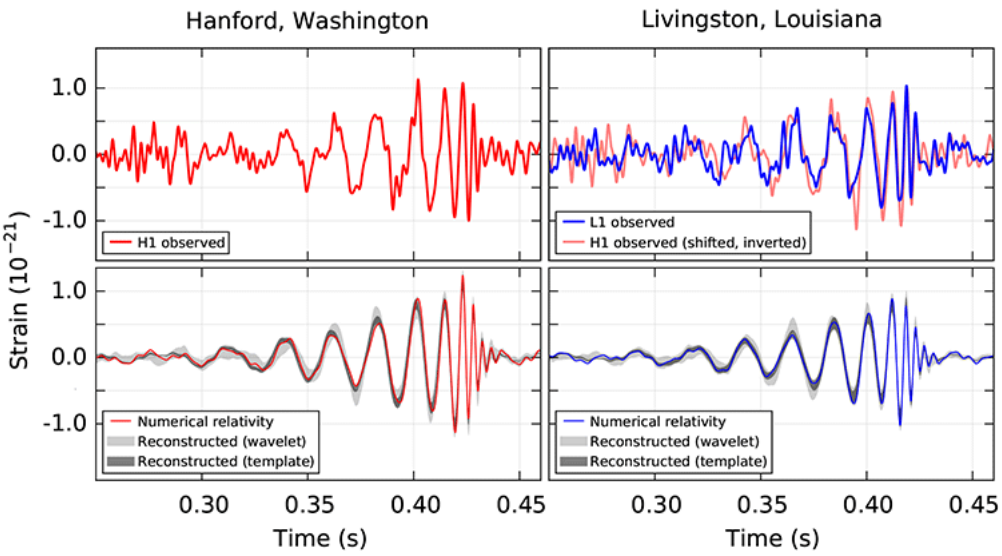

Fig. 1.4: Detected and reconstructed signals of the first gravitational wave event GW150914. Times refer to September 14, 2015 at 09:50:45 UTC.
Credits: LIGO Open Science Center (2016 [14]*).*

account for the relative orientation of the detectors). It is clear that both interferometers have witnessed the same event, confirming the detection.

In the second row, solid red (H1) and blue (L1) lines show a numerical relativity waveform for a system whose parameters are consistent with those calculated from GW150914. Shaded areas show 90 % confidence regions for two independent waveform reconstructions: one (dark gray) models the signal using binary black hole template waveforms, the other (light gray) does not use an astrophysical model, but instead calculates the strain signal as a linear combination of sine-gaussian wavelets. These reconstructions have a 94 % overlap.

The strain signal fluctuates in amplitude and increases in frequency in about 8 cycles over ~ 0.2 s, from 35 Hz to 250 Hz, where it reaches a peak gravitational-wave strain of 1.0×10^{-21}. The decay of the waveform after this maximum is consistent with the damped oscillations of a black hole relaxing to a final stationary Kerr configuration. The event was observed with a signal-to-noise ratio of 24.

The evolution in time of GW151226 signal is similar, even though it has a smaller strain amplitude and a longer time interval. Here, the signal lasted for ~ 1 s over about 55 cycles from 35 Hz to 450 Hz, with a peak amplitude of $\sim 3.4 \times 10^{-22}$. The signal-to-noise ratio was equal to 13.

Some source parameters of the detected signals are summed up in Table 1.1. Parameters evaluation is based on General Relativity waveform models of compact binary coalescence, along with a Bayesian analysis to derive posterior distributions of the source parameters. The estimates of the mass of the final black hole and the total energy radiated in gravitational waves derive from fits to numerical simulations.

The parameters are expressed as median values with 90 % credible intervals that include systematic uncertainties from averaging the results of different waveform models and statistical uncertainties. In the case of GW151226, calibration uncertainties are taken into account as well. Upper/lower error estimates are shown as superscripts/subscripts.

Inferred masses[15] are given in the source frame. Estimates of the masses of the primary and secondary black holes of GW151226 are smaller than those of GW150914, but they are both above $4.5M_\odot$, that is the theoretical maximum mass of a neutron star, with the consequence that both components are identified as black holes.

The radiated gravitational-wave energy equals the amount of energy equivalent to the difference between the sum of the single masses and the mass of the final black hole.

As for the position of the GW sources in the sky, observations have allowed to localize GW150914 and GW151226 respectively in an area of $\sim 600\,\mathrm{deg}^2$ and $\sim 850\,\mathrm{deg}^2$, at a luminosity distance[16] of 410^{+160}_{-180} Mpc and 440^{+180}_{-190} Mpc from Earth.

Source parameters	**GW150914**	**GW151226**
Primary black hole mass	$36^{+5}_{-4}M_\odot$	$14.2^{+8.3}_{-3.7}M_\odot$
Secondary black hole mass	$29^{+4}_{-4}M_\odot$	$7.5^{+2.3}_{-2.3}M_\odot$
Final black hole mass	$62^{+4}_{-4}M_\odot$	$20.8^{+6.1}_{-1.7}M_\odot$
Radiated gravitational-wave energy	$3.0^{+0.5}_{-0.5}M_\odot c^2$	$1.0^{+0.1}_{-0.2}M_\odot c^2$
Frequency interval	[35-250] Hz	[35-450] Hz
Peak gravitational-wave strain	1.0×10^{-21}	$3.4^{+0.7}_{-0.9} \times 10^{-22}$
Signal-to-noise ratio	24	13
False-alarm probability	< 1 in 5×10^6	~ 1 in 10×10^6
Significance	$> 5.1\sigma$	$> 5\sigma$
Duration	$\sim 0.2\,\mathrm{s}$	$\sim 1\,\mathrm{s}$
Luminosity distance	410^{+160}_{-180} Mpc	440^{+180}_{-190} Mpc
Position resolved to	$\sim 600\,\mathrm{deg}^2$	$\sim 850\,\mathrm{deg}^2$

Table 1.1: Experimental estimates of some parameters for the gravitational wave events GW150914 and GW151226.

[15] $M_\odot = 1.989 \times 10^{30}\,\mathrm{kg}$, conventional value of the mass of the Sun.

[16] Luminosity distance D_L of a celestial object is defined as $D_L = \sqrt{\frac{L}{4\pi S}}$ where L and S are the bolometric luminosity and the bolometric flux of the object respectively. The luminosity (W) is the amount of radiated energy per unit of time, while the flux ($\mathrm{W\,m^{-2}}$) is the luminosity per area. Bolometric means integrated over all frequencies.

Chapter 2

Dealing with data

2.1 Flare Advocates

In order to deal with the large amount of data provided continuously by *Fermi*, that uniformly scans the whole sky while operating in the scanning mode, a non-stop monitoring of its data is necessary. This is performed by the *Fermi* LAT Flare Advocate, also known as Gamma-ray Sky Watcher (FA-GSW), activity, belonging to the LAT Instrument Science Operations.

Flare advocates, working on weekly shifts during the whole year, supply a daily human quick-look analysis to all sources detected by the LAT, in particular to transients and high energy flares which may occur any time during the LAT uniform sky scanning. Prompt internal alerts for interesting sources are therefore broadcast to LAT working groups.

The FA-GSW service divides into two task sections:

GSW section Automatic Science Processing (ASP) gives a first, rough location of all point sources direction in a data run (6 h or 1 d). Associations with known sources are then made; if a cluster of photon does not match a known source and at the same time statistic fluctuations are not enough to explain the origin of photons from that point, an additional survey, for example an *ad hoc* multiwavelength campaign, is carried out. Transients and flares, brightness trends and new gamma-ray source candidates are the main topics this investigation is focused on.

FA section FA task consists in fitting with a power-law[1] the energies of photons for each source examined by GSW; sources with a daily flux above $10^{-6}\,\mathrm{ph\,cm^{-2}\,s^{-1}}$ are considered particularly interesting and are thus studied with further analysis[2].

In this way, FA-GSW provides potentially interesting sources to the different LAT groups. Moreover, results are conveyed to the external scientific community — not only to the *Fermi* LAT Collaboration — through Astronomer's Telegrams (ATels), broadcast via the LAT multiwavelength mailing list and published on the Fermi Sky Blog.

Multifrequency observations in international collaboration could then follow FA-GSW investigation, which could represent a starting point for new discoveries as well.

The previous information is included in Bastieri et al. (2011 [5]) and in Ciprini et al. (2012 [8]).

[1] The power law function, that gives the number N of photons with energy E, has the form $\frac{dN}{dE} = N_0(\frac{E}{E_0})^{\gamma}$, where the parameters N_0, γ and E_0 are a prefactor, the so-called photon index and a scale energy respectively. Other models, such a broken power law could be used in particular cases where the simple power law is not suitable.

[2] ph = number of photons.

A typical FA-GSW daily report contains results concerning the data collected by the LAT during four 6 h periods throughout the day and overall during the whole day too. Each period is divided into an "Extragalactic Science" section, showing gamma-ray sources located outside the Milky Way — either because positionally coincident with a known extragalactic source or because their galactic latitude[3] $|B| > 10°$ — and a "Galactic Science" section for sources typically within 10° of the Galactic Plane.

As it can be seen in Fig. 2.1, showing a part of a typical FA-GSW report, each period starts with the counts map provided by ASP, which displays the approximate position of the sources on the celestial sphere by counting how many photons reach the istrument from a certain direction — it has the same characteristics of the map in Fig. 1.2. On the right there is also an exposure map plotting the number of seconds the LAT was observing a given direction of the sky.

Daily run (n. 03003)

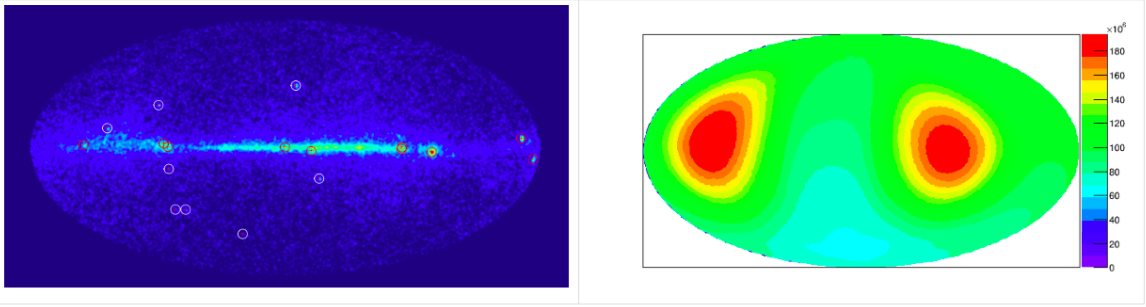

Extragalactic Science	RA(J2000)	DEC(J2000)	L	B	TS	Npred	Flux¤	index	Delta	Type	3FGL comparison	Associations
1510m089	228.3449*	-9.3503*	351.1973*	39.8644*	281	131	2.70±0.30	2.66±0.14	0° 16.8' 0° 53.6'	FSRQ fsrq	2.9: J1512.8–0906 (9.4±0.1)e-7 87: J1513.1–1014 (3.1±1.0)e-8	PKS 1510–08 PKS 1511–100
ASPJ211459p292929	318.7157*	29.5714*	76.5421*	-13.2015*	22	16	0.25±0.09	1.91±0.24	0° 7.1'	fsrq	8.4: J2115.4+2933 (2.9±0.4)e-8	B2 2113+29
ASPJ223119p124704	338.2531*	12.0441*	77.7935*	-38.4077*	102	60	1.29±0.24	2.47±0.19	0° 20.5'	FSRQ	8.0: J2232.5+1143 (1.61±0.05)e-7	CTA 102
ASPJ223421m170933	338.5858*	-17.1591*	43.1988*	-56.8498*	15	15	0.55±0.23	3.12±0.64	0° 25.0'	fsrq	120: J2236.0–1706 (5±2)e-9	PKS 2233–173
3C_454.3	343.2156*	16.2981*	85.9385*	-37.9123*	52	40	0.87±0.21	2.73±0.37	0° 18.8'	FSRQ	0.4: J2254.0+1608 (2.39±0.01)e-6	3C 454.3

Fig. 2.1: Beginning section of the daily run period in a typical FA-GSW report.

A list of the detected sources is then presented in every period. The most significant parameters that describe each of them are explained here.

RA Right ascension (°). $RA \in [0, 360]°$. This is the longitude in equatorial coordinates, measured eastward along the celestial equator, starting from the vernal equinox[4], where $0° \equiv 360°$. J2000 specifies the epoch of reference for the coordinate system, corresponding to the position of the vernal equinox on January 1, 2000, 12:00 UT.

DEC Declination (°). $DEC \in [-90, +90]°$. This is the latitude in equatorial coordinates; 0° corresponds to a point on the celestial equator, while +90° and −90° correspond to the north celestial pole and to the south celestial pole respectively.

L Longitude in galactic coordinates (°). $L \in [0, 360]°$. It is measured eastward along the galactic equator, starting from the galactic center (where $0° \equiv 360°$).

[3] See below.

[4] One of the two intersections of the ecliptic with the celestial equator, where the Sun is on the date of vernal equinox.

B Latitude in galactic coordinates (°). $B \in [-90, +90]°$. 0° corresponds to a point on the galactic equator, while +90° and −90° correspond to the north galactic pole and to the south galactic pole respectively.

TS The Test Statistic evaluated by the maximum likelihood ratio test. It is computed as $-2\ln(\frac{\mathcal{H}_{0,\max}}{\mathcal{H}_{\max}})$, where $\mathcal{H}_0$ is the null hypothesis of not having a source in the given (RA, DEC) and $\mathcal{H}$ is the alternate hypothesis, both maximized in the maximum likelihood ratio test. The greater the TS, the greater the probability that a source of gamma rays was active in our time window in the given direction. By Wilks' Theorem it follows, in our case, a χ^2 distribution with 2 degrees of freedom; a good approximation of the significance of the source is thus $\sigma = \sqrt{TS}$.

Npred Total number of gamma rays from the source predicted by the model.

Flux Photons flux measured, in units of $10^{-6}\,\mathrm{ph\,cm^{-2}\,s^{-1}}$ in the [0.1-300] GeV energy band.

Index Photon power law index γ.

Delta Distance in arcminutes from the sources in the *Fermi* catalogs within 1°.

Type Type of celestial object, if a positional coincidence exists (an entry in the *Fermi* catalogs which lies within 1° of the given direction).

3FGL comparison Flux ratio between the detected source and the association for the *Fermi* catalogs (typically the 3FGL is used).

Associations Associations, if any, of the *Fermi* catalog entry.

It could be present also an "Unidentified" section for those sources that have not been matched with known objects. Little changes in entries name or in the order may exist depending on the Flare Advocate on duty.

2.2 HEALPix: pixelation of the sphere

HEALPix (Hierarchical Equal Area iso-Latitude Pixelation) is a method of pixelation of the sphere. Amongst the others, several astrophysics research groups employ this useful tool in order to deal with data sets referring to positions on the celestial sphere centered on the observer and therefore to create full-sky maps.

Since it is not possible to map the experimental values of a signal to every mathematical point on the sphere, because of the limited resolution of the instruments, the purpose is to discretize it: the surface of the sphere is represented as a tessellation consisting of a certain number of solid angles, each of them related in bi-univocal correspondence with an actual direction in the sky. Obviously, the amount of these pixels has to be sufficiently high to well-reproduce the resolution of the instruments. Any function with the sphere as domain will then assume discrete values, allowing numerical analyses.

The need for a technique like this, instead of, more simply, discretizing a flat surface which reproduces the sky, is due to the fact that bi-univocal correspondence would not be satisfied. In fact, considering for example a map projection like that in Fig. 1.2, it is clear that the points on the equator at opposite extremities (+180° on the left and −180° on the right) are the same point on the celestial sphere. Moreover, the average position of regions sorrounding them would be $\sim 0°$, even if definitely it is not, since 0° is located at the center of the map.

Anyway, the function mapping the points on the flat surface to the points on the sphere would not be a one-to-one function, and the inverse operation even not a function, arising problems concerning how to deal with signals related to some directions in the sky.

HEALPix, as other sphere-pixelation methods[5], represents a possible way to solve these issues: *first*, directions are identified and numbered on the two-dimensional surface of the sphere and only *then* they are mapped in one-dimensional number arrays, ready for analysis. In *addition*, a two-dimensional projection on the plane, such that in Fig. 1.2, can be created in order only to *display*, not to *evaluate*, some features of the data, such as the distribution of gamma-ray emission from the sky.

According to Healpix — Credits web page (2016, [12]), the basic idea of HEALPix came from K.M. Górski at the Theoretical Astrophysics Center (TAC)[6] in Copenhagen at the beginning of 1997 and was implemented together with E. Hivon in the spring of the same year. Then it was further developed in collaboration with B.D. Wandelt, F.K. Hansen, A.J. Banday and M. Bartelmann, leading to the first release of HEALPix software, Version 1.10. Version 3.30 is the current release.

The project depends entirely on the voluntary contributions of the mentioned and many other individuals and on suggestions from the users as well.

HEALPix software was firstly used by NASA's WMAP mission[7] and currently by ESA's Planck mission[8], with the aim of investigating the Cosmic Microwave Background (CMB). Data from both current and past missions such as NASA's WISE[9] and COBE[10] are now stored in HEALPix format. Several other astronomy and cosmology research programs, including *Fermi* mission, employ HEALPix, but this software is useful in geophysics, atomic and nuclear physics applications as well.

HEALPix software package, including documentation and examples, is available in C, C++, Fortran90, IDL, Java and Python, which is the one we have used, called Healpy (Version 1.9.1).

2.2.1 How HEALPix works

The full explanation of HEALPix is available in *The HEALPix Primer* (Górski et al. 2015 [11]). According to it, HEALPix pixels are exactly equal area quadrilaterals of varying shapes. The base-resolution HEALPix pattern consists of 12 pixels in three rings: 4 in the equatorial ring, 4 around the north pole and 4 around the south pole. Each of them is then divided into four pixels, each of these again into four pixels and so on, in order to achieve increased-resolution patterns, as shown in Fig. 2.3. Every pixel is associated with a number that univocally identifies its position on the sphere.

The key features of this pixelation mechanism are included in the terms of the acronym HEALPix:

Hierarchical The first term refers to the division pattern itself, with a base "parent" pixels and consecutive "daughter" and "granddaughter" pixels and so on. Moreover, pixels are labelled in a hierarchic way, with the numbering method following the tree structure in which the pixels are organized. In order to understand what hierarchical

[5]Other alternative hierarchical grids are the Quadrilateralized Spherical Cube, which was used for the COBE data, and the Hierarchical Triangular Mesh (HTM).

[6]No longer operating.

[7]Wilkinson Microwave Anisotropy Probe, operating between 2001 and 2010.

[8]Launched in 2009.

[9]Wide-field Infrared Survey Explorer, launched in 2009, with the goal of imaging the entire sky in the infrared.

[10]Cosmic Background Explorer, that had been preceding WMAP and Planck between 1989 and 1993 in the CMB detection.

numbering implies, the example of a partition of a squared shape with a quadrilateral tree structure may be helpful (see Fig. 2.2).

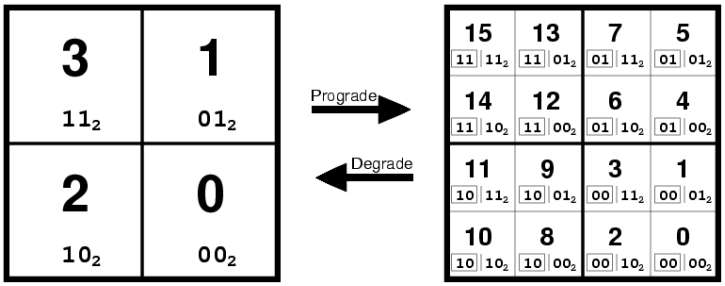

Fig. 2.2: Hierarchical numbering in a quadrilateral tree structure, from the base-resolution pattern on the left to the increased-resolution pattern on the right.
Credits: The HEALPix primer (Górski et al. 2015 [11]*).*

Every quadrilateral area in the base-resolution pattern on the left is labelled with two bits. In the increased-resolution pattern on the right, each of the previous pixel is divided into two sub-pixels. Now four bits are needed to indicate each pixel and every sub-pixel in the same base-resolution pixel has the same first two bits (boxed). This is a basic property that does turn out to be useful in computational analysis: pixels that are nearby in a multi-dimensional space[11], the so-called "near-neighbors", are also nearby in the tree structure of the data base. In this way they are easily traced in the computer RAM and all computing processes involving them can be optimally carried out.

Equal Area All pixels are exactly equal area quadrilaterals; this is a basic requirement, since in this way each of them is of the same importance as the others in signal sampling. Nevertheless, because of the need for covering the whole surface of the sphere, they unavoidably differ in shape. Under suitable hypothesis, however, all pixels can be assumed identical, for the purpose of simplifying some computational evaluations. The area Ω_{pix} of each pixel satisfies $\Omega_{pix} = \frac{\pi}{3N_{side}^2}$ (Górski et al. 2005 [10]).

iso-Latitude The centers of the pixels (marked with a dot in Fig. 2.3) belonging to the same ring share the same latitude, that it is of essential importance for computational speed of all operations that involve the evaluation of Fourier transforms with spherical harmonics, widely used in the CMB research.

The key parameters involved in the partition of the sphere are the following:

$\boldsymbol{N_{side}}$ Number of divisions along the side of a base-resolution pixel. It equals 1 in the base-resolution pattern, 2 in the pattern with 4 pixels in each base-resolution pixel and so on. As a consequence, it can be only a power of 2: $N_{side} = 2^k$, with $k \in \mathbb{Z}$. k is sometimes called the *order* of the pattern, while N_{side} is the *grid resolution parameter*, as the resolution increases with it.

$\boldsymbol{N_{pix}}$ Total number of pixels. $N_{pix} = 12 \cdot N_{side}^2$.

$\boldsymbol{N_{ring}}$ Number of iso-latitude rings. $N_{ring} = 4N_{side} - 1$.

$\boldsymbol{p}$ The index each pixel is labelled with. $p \in [0, N_{pix} - 1]$.

[11] Here the two-dimensional square or sphere.

Moreover, all rings in the equatorial zone, namely the region of the sphere including rings adjacent to the upper and lower corners of the base-resolution pixels, are divided into the same number of pixels, $N_{eq} = 4N_{side}$. Within the polar cap regions the number of pixels decreases, with increasing distance from the equatorial zone, from ring to ring by 1 pixel inside each quadrant. All pixels on the same ring are equidistant in azimuth.

Furthermore, HEALPix supports two different numbering schemes for the pixels, the RING scheme and the NESTED scheme (see Fig. 2.4).

In the RING scheme, pixels are numbered along each iso-latitude ring, from the north pole to the south pole. Calculations with spherical harmonics are easily implemented with this scheme.

In the NESTED scheme, a tree structure based on the twelve base-resolution pixels is used, in a way similar to that of the square shape with a quadrilateral structure in Fig. 2.2. The numbering starts from the pixels in the north polar cap and ends with south pole pixels. In the $N_{side} = 2$ pattern, the numbering inside each of the base-resolution pixels starts from its lower sub-pixel, continues with the central sub-pixels from the right one and ends with the upper sub-pixel. In the $N_{side} = 4$ pattern, each of the previous sub-pixels splits in other four sub-sub-pixels with the same numbering rules, as it is better understood in Fig. 2.4, and so on for greater-resolution patterns. Near-neighbor searches are easily conducted with this scheme.

The NESTED scheme best reflects the hierarchical structure and numbering of the pixelation, while the RING scheme is not actually hierarchical by its nature. Nevertheless, fast routines useful for easily switching between them are included in the software. The NESTED is the scheme mainly used in order to deal with gamma-ray emission data collected by *Fermi*, since evaluations involving spherical harmonics are not carried out and instead near-neighbor searches are fundamental.

In both schemes, the two-dimensional distribution of discrete area elements on the sphere can be mapped in a one-dimensional, integer pixel number array useful for further analysis.

It has been mentioned above that any function on the sphere is discretized. More precisely, a pixelated signal $f(p)$ is the average within each pixel p of the values of the underlying signal inside the pixel:

$$f(p) = \int d\boldsymbol{u}\omega_p(\boldsymbol{u})f(\boldsymbol{u})$$

where $d\boldsymbol{u}$ is the surface element of the pixel, $\omega_p = 1/\Omega_{pix}$ inside the pixel and $\omega_p = 0$ outside, so that $\int d\boldsymbol{u}\omega_p(\boldsymbol{u}) = 1$. Then the function $f(p)$ can, if needed, be expanded in spherical harmonics.

The need for equal area pixels is now better understood: for example, if Ω_{pix} differs from pixel to pixel and assuming that the original signal has the same uniform value over two different pixels, then the average signal, instead of showing equivalence between them, would be greater in the pixel with the smaller surface.

Moreover, it is clear that, if the original signal has values that highly vary inside each pixel, the outcome would be a degradation and smoothing of the original signal. In order to avoid this effect as much as possible, the size of the pixels has to be sufficiently small compared to the resolution of the instruments: N_{pix} has at least not to be lower than the number of divisions detectable by the instrument. As an example, an angular resolution[12] of $10'$ requires at least $N_{pix} = 10^7$, that means $N_{side} = 2^{10} = 1024$. On the other hand,

[12]Here expressed as the Full Width at Half Maximum (FWHM) of the distribution that describes experimental data.

computational cost grows with increasing N_{side}, so a compromise should be found.

Finally, in order to deal with astronomical objects detected in certain directions in the sky, HEALPix defines the coordinates on the sphere, as shown in Fig. 2.5, as:

ϕ Azimuth (rad). $\phi \in [0, 2\pi]$. It is the longitude, measured eastward along the celestial equator, starting from the vernal equinox, where $0 \equiv 2\pi$.

θ Polar angle (rad). $\theta \in [0, \pi]$. It is the colatitude, measured southward starting from the z-axis, with $\theta = 0$ corresponding to the north celestial pole and $\theta = \pi$ to the south celestial pole.

N.B. The azimuth and the polar angle are not the same of the equatorial coordinates that FA-GSW make use of. ϕ corresponds to RA, but $\theta = \pi/2 - DEC$(rad).

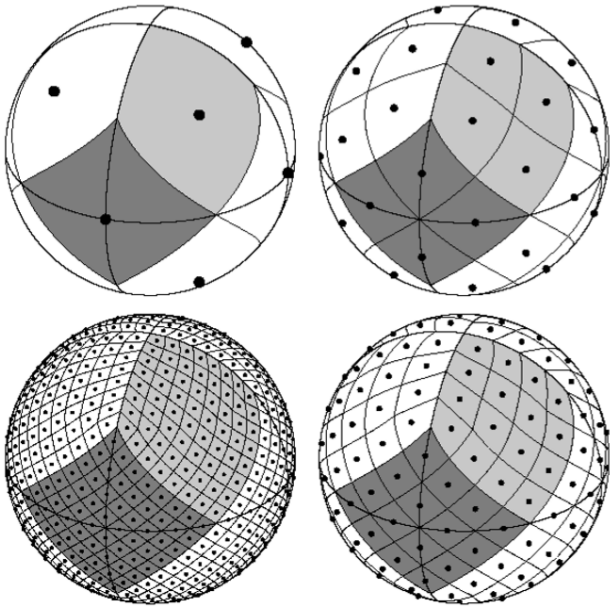

Fig. 2.3: The HEALPix tessellation of the sphere in four increasing-resolution patterns, starting from the base-resolution pattern in the upper left panel. Clockwise from the latter: $N_{side} = 1, 2, 4, 8$; $N_{pix} = 12, 48, 192, 768$; $N_{ring} = 3, 7, 15, 31$; $N_{eq} = 4, 8, 16, 32$.
Credits: The HEALPix primer (Górski et al. 2015 [11]*).*

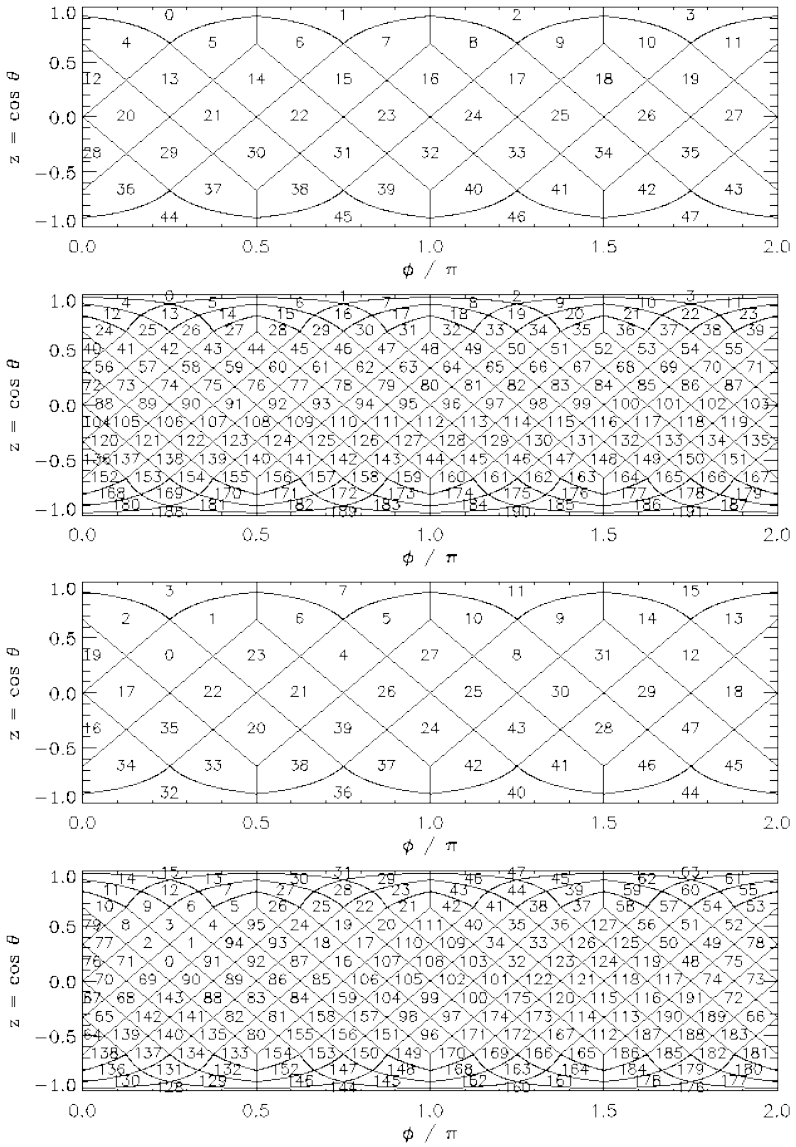

Fig. 2.4: Cylindrical projection of the sphere with RING (in the first two panels) and NESTED (in the second two panels) numbering schemes. The grid resolution parameter N_{side} equals 2 and 4 in the top and bottom panels respectively for each scheme.
In the cylindrical projection, meridians are mapped to equally spaced vertical lines, while parallels to horizontal lines, as they were projected onto a cylinder wrapping the Earth with its axis parallel to the terrestrial rotation axis and then unrolled.
Credits: The HEALPix primer (Górski et al. 2015 [11]*).*

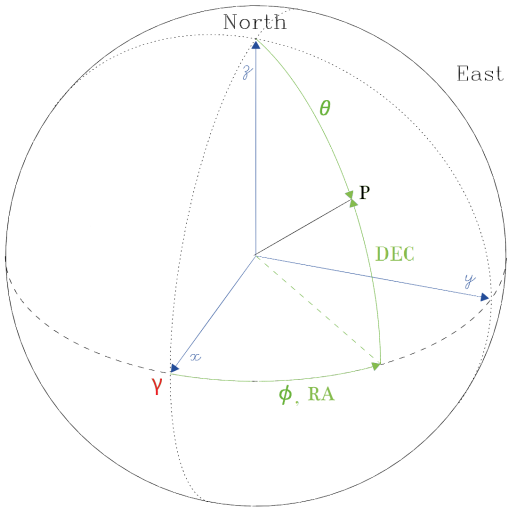

Fig. 2.5: HEALPix and equatorial coordinates of a point P on the celestial sphere. γ, shown in red, is the vernal equinox.

Chapter 3

The "banana plots" and the tool

3.1 GW sky location probability maps

For each of the gravitational wave signals detected by LIGO's interferometers, a sky probability map is produced. The map contains, for each direction in the sky, the posterior probability that the GW source is located there. The projection of the map on the two-dimensional celestial sphere is often called "banana plot", since it shows a banana-shaped area of the sky whose contours include the 90 % confidence level probability region for that GW event. This band of the sky is very large: as it was already mentioned in Section 1.2.2, the two detected events GW150914 and GW151226 have been localized in an area of $\sim 600\,\mathrm{deg}^2$ and $\sim 850\,\mathrm{deg}^2$ respectively.

According to Abbott et al. (2016c [3]), four different algorithms are used in order to obtain as many different sky maps: cWB, LIB, BAYESTAR and LALInference. The last one, modeling the data with a compact binary coalescence (CBC) waveform, is the most accurate method for CBC signals, even though it takes the longest time, while cWB, LIB and BAYESTAR lead to a rapid localization. Since GW150914 and GW151226 signals are related to CBC events, the LALInference map is considered the most accurate and final localization method for these sources, although all the maps agree qualitatively. For this reason, our tool for the search for gamma-ray counterparts is using LALInference data.

LALInference algorithm provides a HEALPix-FITS file containing the GW probability values. FITS is an acronym for "Flexible Image Transport System" and it is the standard format for writing astronomical data files, endorsed by NASA and the International Astronomical Union (IAU). It is useful in order to store data in multi-dimensional arrays and tables, to analyze them and to insure data portability.

From the LALInference FITS file, an array cointaining the GW probability for each pixel that corresponds to a discretized direction in the sky (that is the sky probability map) can be extracted with Healpy, the Python library belonging to the HEALPix distribution package. In particular, the function able to perform this task is the `read_map` function, that reads the FITS file and returns an array containing the HEALPix map, here called `gwmap`. Its syntax, with the fundamental parameters to be specified as arguments, is

```
gwmap=read_map(fits_name, field=None, dtype=np.float32,
nest=True, hdu=1)
```

where `fits_name` is the name of the FITS file under consideration.

`field=None` means that all columns of the file are read in, that is all its data are collected. `dtype=np.float32` corresponds to the data type used in the file, in this case single precision floats. `nest=True` returns the map in the NESTED ordering scheme (if

`False` in the RING ordering scheme, but LALInference files are usually written in the former scheme). `hdu=1` stands for the header number to look at in the file[1].

Once `gwmap` is read, it is possible to project it onto a two-dimensional surface representing the celestial sphere, for instance a Mollweide projection[2], through the `mollview` function. Its basic format appears as

```
mollview(map_name, coord='C', nest=True)
```

where `map_name` is the name of the array containing the map, here `gwmap`. `coord='C'` sets the coordinate system to be used: `C` stands for celestial coordinates, that is the same of equatorial coordinates, since the sky maps are represented in the FITS files in equatorial frame; other available systems are `G` and `E`, corresponding to galactic and ecliptic[3] coordinates respectively. `nest=True` has the same meaning explained above.

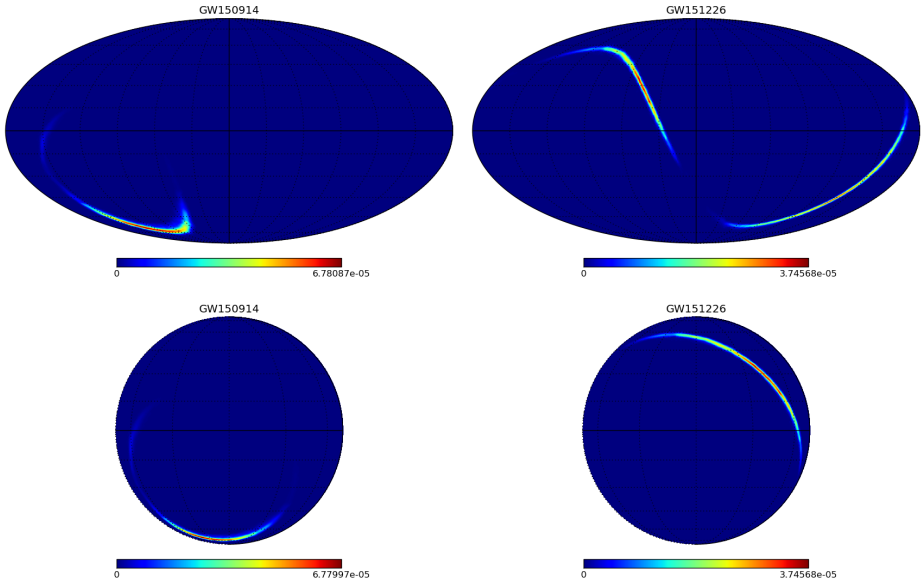

Fig. 3.1: Mollweide (top panels) and Ortographic (bottom panels) projections of GW150914 (left column) and GW151226 (right column) sky location probability maps in equatorial coordinates. A graticule shows meridians and parallels with 30° and 15° intervals between the former and the latter respectively. Here $N_{side} = 512$, meaning $N_{pix} = 3\,145\,728$. *Credits: data from the LIGO Open Science Center (2016* [14] [15]*).*

Mollweide projections of GW150914 and GW151226 maps are visible in the top panels of Fig. 3.1. The maps are in equatorial coordinates, with the center of the Galaxy at the center of the map and *RA* increasing to the left (eastward). The banana shape is more visible with a different choice of the projection, for instance an Orthographic projection[4], that can be plotted with the `orthview` function, with parameters similar to the `mollview` function.

[1]Headers are file blocks containing information about structure of the file and data characteristics such as dimension, format, as well as date and time of the observations and other features.

[2]Pseudo-cylindrical equal-area projection. The central meridian is a straight line, 90° meridians are circular arcs and all other meridians are equally spaced elliptical arcs. Parallels are unequally spaced straight lines, parallel to each other. The scale is not distorted only along the latitudes 40°44′ N and S. (Snyder 1987 [18])

[3]Similar to equatorial coordinates, with ecliptic and ecliptic poles replacing celestial equator and celestial poles respectively.

[4]Azimuthal non equal-area projection. It presents no distortion only at the center, but directions from the center are true. Only one hemisphere can be shown at a time. (Snyder 1987 [18])

This second type of maps is visible in the bottom panels of Fig. 3.1, showing the side of the sphere with the coordinates of the point at the center being $(RA, DEC) = (90, 0)^\circ$ and RA increasing to the left (eastward). Different probability values are displayed with a false color scale, from blue (minimum probability) to red (maximum probability). The highest probability values detected in GW150914 and GW151226 events amount to 6.78×10^{-5} and 3.74×10^{-5} respectively.

3.2 Follow-up EM observations. The basic code of the tool

Celestial objects that could be probably associated with emission of gravitational waves are CBC events and tight binaries composed of two neutron stars (NSs), or two black holes (BHs) — such as GW150914 and GW151226 — or a NS and a BH. All these systems should emit gravitational radiation, resulting in a runaway orbital decay. Moreover, in binary systems including at least one neutron star, electromagnetic (EM) signatures are expected due to energetic outflows at different timescales and wavelengths: a short-duration GRB[5], lasting less than $\sim 2\,\mathrm{s}$, and following X-ray, optical and radio emissions of hours-to-days duration could be detected, along with, for example, coherent radio bursts lasting milliseconds and appearing several seconds prior to the merger or tens of minutes after it. In addition, neutrinos emission is also expected.

In the case of a binary black hole (BBH) merger in vacuum, classical General Relativity predicts no EM or particle emission. Only supermassive BBHs placed in environments such as galactic centers may produce these types of emission, due to interactions with large magnetic fields and high gas densities.

Within two days of GW150914 being detected, alerts and initial sky probability maps were sent to collaborations and teams that deal with EM sky observations, included *Fermi* LAT and GBM. Over the following three months, observations of a wide range of wavelengths, from radio to gamma rays, were performed by 25 satellites and ground-based telescopes. The localization region for GW150914 was outside the *Fermi* LAT Field of View at the time of the gravitational wave signal, but the observations started $\sim 70\,\mathrm{min}$ after the trigger (Ackermann et al. 2016 [4]) and the entire localization continued to be observed every $\sim 3\,\mathrm{h}$ on its orbit. However, no significant EM signals were associated with GW150914, accordingly to its BBH nature. The information about its nature and updated sky maps were sent out respectively 20 days and 4 months after the event, but future alerts are expected to be issued within tens of minutes with more details about the signal type and more rapid updates of the maps.

The importance of the searches for EM signatures is related, for example, to the identification of the galaxy that hosts the GW event. The number of galaxies whose position in the sky is included within the 90 % credible area of the LALInference sky map and within the 90 % confidence interval distance is $\sim 10^5$. Such a number makes it impossible to identify the host galaxy in the absence of an EM counterpart detection.

The first EM follow-up program, in preparation for advanced detector operations, was carried out in 2009 and 2010 by iLIGO, Virgo detectors and several EM collaborations.

The previous information is included in Abbott et al. (2016c [3]).

Our research is trying to provide the world-wide community of observatories with prompt alerts any time a gamma-ray counterpart of a gravitational wave candidate event is observed by the *Fermi* LAT. Therefore, we are developing a tool that will report, for each gamma-ray source detected by the LAT, the probability, inferred from the LIGO sky maps,

[5] See Section 1.1.2.

that it represents a source of gravitational waves as well, with relation to the GW event under consideration.

The implementation of the tool is still in progress; it will be expanded soon to include, for instance, the posterior probability of a source being compatible with a neutrino event.

The basic functioning of the tool requires as input the list of the coordinates of the gamma-ray sources to be analyzed, provided in FA-GSW reports, and the LALInference FITS file. The GW sky location probability map, `gwmap`, is extracted with the `read_map` function, as explained above. The coordinates of the gamma-ray sources, say a couple of `ra` and `dec` for each source, usually expressed in the equatorial coordinate system and in degrees, have to be converted to Healpix coordinates, say `ra_rad` and `dec_rad`, using a code similar to

```
ra_rad = [radians(x) for x in ra]
dec_rad = [radians(90.-x) for x in dec]
```

where `ra_rad` $= \phi$ (rad), `dec_rad` $= \theta$ (rad), `ra` $= RA$ (°) and `dec` $= DEC$ (°) are arrays including each type of coordinates respectively[6]. A `for` cycle is needed in order to iterate the conversion for each element of `ra` and `dec`. `radians` is a function belonging to the `math` Python module, that implements the conversion from degrees to radians.

The next step consists in assigning to each couple of `ra_rad` and `dec_rad` the index of the pixel, p, corresponding to the direction of the gamma-ray source. This can be performed by the `ang2pix` function, with the essential syntax

```
ipix = ang2pix(nside, dec_rad, ra_rad, nest=True)
```

where `nside` is the N_{side} parameter of the GW map, previously obtained with the `nside = healpy.get_nside(gwmap)` command, that reads it from `gwmap`. `ipix` is the array of p indexes for each gamma-ray source.

The final stage contains a command similar to

```
gwprob = [gwmap[x] for x in ipix]
```

that fills the new array `gwprob` with those values from `gwmap` that correspond to each element of `ipix`. The final output is therefore an array of the probability of GW emission associated to every gamma-ray source. This will then become an additional column in the FA-GSW report under consideration.

Moreover, in order to immediately visualize the results, a map projection similar to those of Fig. 3.1 could be created, with the addition, for instance, of points indicating the position of the gamma-ray sources in the sky. In this way, in the 90 % GW confidence level probability region the interesting sources would be visible.

In conclusion, the basic code of the tool appears as follows.

```
import healpy
import numpy as np #python package for scientific computing
from math import radians

fits_name = '...'
gwmap = healpy.read_map(fits_name, field=None, dtype=np.float32,
nest=True, hdu=1)

sources = [[..., ...], [..., ...], ...]  #2d list with [ra, dec]
```

[6]See Section 2.2.1 for the comparison between FA-GSW and HEALPix coordinate systems.

```
ra, dec = zip(*sources) #to obtain two 1d separate lists

ra_rad = [radians(x) for x in ra]
dec_rad = [radians(90.-x) for x in dec]

nside = healpy.get_nside(gwmap)
ipix = healpy.ang2pix(nside, dec_rad, ra_rad, nest=True)
gwprob = [gwmap[x] for x in ipix]

output = zip(ra, dec, gwprob) #output in degrees
```

An example of the typical output of our tool is shown in Fig. 3.2, that is the same of Fig. 2.1 with the addition of a column presenting the GW probability evaluated from the GW150914 event. The minimun probability threshold useful to recognize likely gamma-ray counterparts can be set between 10^{-8} and 10^{-7}, since these are the typical probability values corresponding to the contours of the banana plot. For all sources included in the beginning section of the report in Fig. 3.2, the order of magnitude of the probability is equal, instead, to 10^{-22} or 10^{-23}, that are standard values outside the banana and thus do not correspond to gravitational wave counterparts[7].

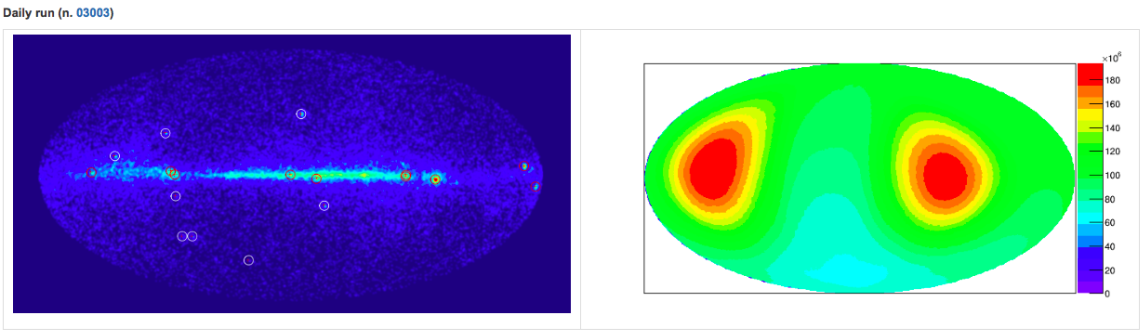

Extragalactic Science	RA(J2000)	DEC(J2000)	L	B	TS	Npred	Flux¤	index	Delta	Type	3FGL comparison	Associations	GW Prob
1510m089	228.3449*	-9.3503*	351.1973*	39.8644*	281	131	2.70±0.30	2.66±0.14	0° 16.8' 0° 53.6'	FSRQ fsrq	2.9: J1512.8−0906 (9.4±0.1)e-7 87: J1513.1−1014 (3.1±1.0)e-8	PKS 1510−08 PKS 1511−100	2e-22
ASPJ211459p292929	318.7157*	29.5714*	76.5421*	-13.2015*	22	16	0.25±0.09	1.91±0.24	0° 7.1'	fsrq	8.4: J2115.4+2933 (2.9±0.4)e-8	B2 2113+29	4e-22
ASPJ223119p124704	338.2531*	12.0441*	77.7935*	-38.4077*	102	60	1.29±0.24	2.47±0.19	0° 20.5'	FSRQ	8.0: J2232.5+1143 (1.61±0.05)e-7	CTA 102	7e-22
ASPJ223421m170933	338.5858*	-17.1591*	43.1988*	-56.8498*	15	15	0.55±0.23	3.12±0.64	0° 25.0'	fsrq	120: J2236.0−1706 (5±2)e-9	PKS 2233−173	2e-22
3C_454.3	343.2156*	16.2981*	85.9385*	-37.9123*	52	40	0.87±0.21	2.73±0.37	0° 18.8'	FSRQ	0.4: J2254.0+1608 (2.39±0.01)e-6	3C 454.3	8e-22

Fig. 3.2: Beginning section of the daily run period in a typical FA-GSW report, with the addition of the GW probability.

[7]Since these values, related to non interesting sources, are so small, the threshold value can be set even at 10^{-10}.

Conclusions

Since the beginning of *Fermi* mission in 2008, a wide variety of thousands of celestial objects, both inside and outside the Milky Way, that emit electromagnetic waves in the gamma-ray band has been detected, remarkably broadening the catalogs of sources detected by previous telescopes. On the other hand, space-time fluctuations related to the emission of gravitational waves during the final phase of the merging between two black holes were observed just a year ago. The strong points of the pair-conversion telescope LAT are its large Field of View and its "scanning" observation mode, while the twin LIGO's laser interferometers lately reached the expected sensitivity needed to detect gravitational waves. Nevertheless, great efforts still have to be made to solve several questions concerning gamma-ray production, black holes properties and the limits of General Relativity.

The activity of Flare Advocates is of paramount importance in order to keep a continuous monitoring of the gamma-ray sky, in particular of those transients that may occur any time throughout the LAT's orbit around Earth, and to identify the most interesting sources. Thanks to the cooperation with LIGO, the new aim to link gamma rays to gravitational waves makes all this even more exciting.

The essential instrument we have used in the elaboration of the tool, HEALPix, does not act only as a mathematical algorithm for the tessellation of the sphere into discretized area elements, but really makes computational analyses of experimental data sufficiently fast and provides a lot of useful utilities such as pixel manipulation and maps visualization.

Our basic tool represents only a small, initial contribution to this vast research. Additional features are going to be added to the tool, in order to hopefully enable the detection of neutrinos and perhaps of other particles from gravitational wave sources. Moreover, *Fermi* is only one of the several missions aiming at finding electromagnetic counterparts to gravitational wave events. Future new gravitational wave detectors and improvements to LIGO's and to already existing interferometers will significantly increase the efficiency of searches for electromagnetic emissions.

The extended tool is going to be used during O2 LIGO's next run, starting within few days. New thrilling gravitational wave events are hopefully awaited in the near future.

Bibliography

[1] Abbott B.P. et al. (LIGO Scientific Collaboration and Virgo Collaboration) (2016a), *Observation of Gravitational Waves from a Binary Black Hole Merger*, Phys. Rev. Lett. 116, 061102.

[2] Abbott B.P. et al. (LIGO Scientific Collaboration and Virgo Collaboration) (2016b), *GW151226: Observation of Gravitational Waves from a 22-Solar-Mass Binary Black Hole Coalescence*, Phys. Rev. Lett. 116, 241103.

[3] Abbott B.P. et al. (LIGO Scientific Collaboration, Virgo Collaboration et al.) (2016c), *Localization and Broadband Follow-up of the Gravitational-wave Transient GW150914*, The Astrophysical Journal Letters 826 (1), L13.

[4] Ackermann et al. (2016), *Fermi-LAT Observations of the LIGO Event GW150914*, The Astrophysical Journal Letters 823 (1), L2.

[5] Bastieri D., Ciprini S., Gasparrini D. (Fermi LAT Collaboration) (2011), *Fermi-LAT View of Bright Flaring Gamma-Ray Blazars*, J. Astrophys. Astr. 32, 169-172.

[6] Berger E. (2014), *Short-Duration Gamma-Ray Bursts*, Annual Review of Astronomy and Astrophysics 52, 43-105.

[7] Charles E. et al. (Fermi LAT Collaboration) (2016), *Sensitivity Projections for Dark Matter Searches with the Fermi Large Area Telescope*, Physics Reports 636, 1-46.

[8] Ciprini S., Gasparrini D., Bastieri D. (Fermi LAT Collaboration) (2012), *Fermi LAT Flare Advocate Activity*, proceedings IAU Symposium 285 2011 (*New Horizons in Time-Domain Astronomy*), 294-295.

[9] Fermi Science Support Center (2016) (*http://fermi.gsfc.nasa.gov/ssc/data/access/lat/4yr_catalog/*).

[10] Górski K.M., Hivon E., Banday A.J., Wandelt B.D., Hansen F.K., Reinecke M., Bartelman M. (2005), *HEALPix — a Framework for High Resolution Discretization, and Fast Analysis of Data Distributed on the Sphere*, The Astrophysical Journal 622, 759-771.

[11] Górski K.M., Wandelt B.D., Hivon E., Hansen F.K., Banday A.J., *The HEALPix primer* (2015 revision), available at *http://healpix.sourceforge.net/documentation.php*.

[12] HEALPix — Credits (2016) (*http://healpix.sourceforge.net/credits.php*).

[13] LIGO Lab | Caltech | MIT (*https://www.ligo.caltech.edu*).

[14] LIGO Scientific Collaboration, "LIGO Open Science Center release of GW150914" (2016) DOI 10.7935/K5MW2F23. *This research has made use of data, software and/or web tools obtained from the LIGO Open Science Center (https://losc.ligo.org), a service of LIGO Laboratory and the LIGO Scientific Collaboration. LIGO is funded by the U.S. National Science Foundation.*

[15] LIGO Scientific Collaboration, "LIGO Open Science Center release of GW151226" (2016) DOI 10.7935/K5H41PBP. *This research has made use of data, software and/or web tools obtained from the LIGO Open Science Center (https://losc.ligo.org), a service of LIGO Laboratory and the LIGO Scientific Collaboration. LIGO is funded by the U.S. National Science Foundation.*

[16] Michelson P.F., Atwood W.B., Ritz S. (2010), *Fermi Gamma-ray Space Telescope: High-Energy Results from the First Year*, Rept. Prog. Phys. 73, 7 (074901).

[17] NASA — Fermi Spacecraft and Instruments (2008) (*http://www.nasa.gov/mission_pages/GLAST/spacecraft*).

[18] Snyder J.P. (1987), *Map projections: A working manual*, U.S. Geological Survey Professional Paper 1395, Washington, DC: United States Government Printing Office.